

Ab initio prediction of anomalous Hall effect in antiferromagnetic CaCrO₃

Thi Phuong Thao Nguyen^{1,2} and Kunihiko Yamauchi^{1,2}

¹*Institute of Scientific and Industrial Research, Osaka University,
8-1 Mihogaoka, Ibaraki, Osaka, 567-0047, Japan*

²*Department of Precision Engineering, Graduate School of Engineering,
Osaka University, 2-1 Yamadaoka, Suita, Osaka 565-0871, Japan*

(Dated: March 30, 2023)

While the anomalous Hall effect takes place typically in ferromagnets with finite magnetization, large anomalous Hall conductivity in *noncollinear* antiferromagnetic systems has been recently observed and attracted much attention. In this study, we predict the anomalous Hall effect in perovskite CaCrO₃ as a representative of ‘*collinear*’ antiferromagnetic materials. Our result shows that the C-type antiferromagnetic ordering generates the sizable anomalous Hall conductivity. Based on symmetry analyses, we show that the antiferromagnetic order parameter belongs to the same irreducible representation as the ferromagnetic order parameter in the nonsymmorphic space group, allowing the non-vanishing Berry curvatures in k space. By performing first-principles density-functional theory calculations, we find that the Berry-curvature ‘*hot spots*’ lie along the gapped nodal lines where spin-orbit coupling induces the spin splitting of Cr-3d bands near the Fermi energy and enhances the anomalous Hall effect in CaCrO₃.

I. INTRODUCTION

The anomalous Hall effect (AHE) is traditionally considered to be proportional to net magnetization and therefore appears only in ferromagnetic (FM) materials [1]. Nevertheless, recent studies have revealed that large anomalous Hall conductivity (AHC) emerges in Kagome antiferromagnetic (AFM) materials such as Mn₃Ge and Mn₃Sn regardless of their small net magnetization [2–10]. Such a large AHC in antiferromagnets may work as a readout for a spintronic device accompanied by their ultra-fast spin dynamics and insensitivity to external magnetic fields, whereas only a few AFM materials have been studied in this context [11–15].

Suzuki *et al.* have investigated the magnetic symmetry by introducing a magnetic cluster extension; the non-collinear AFM structure in Mn₃Sn is characterized by the cluster octupole moment, which belongs to the same irreducible representation as the collinear ferromagnetic ordering. This explains why the noncollinear antiferromagnetic order can induce an AHC despite its vanishingly small dipole magnetization [16]. The same approach has been later applied to antiperovskite manganese nitrides such as Mn₃PtN, where their magnetic octupole non-collinear AFM states allow for inducing the large AHC as well [17].

Recent theoretical development provides the topological formulation of the intrinsic AHE in terms of the Berry phase associated with the Bloch wave functions in solids [18]. While the AHC can be calculated by integrating the Berry curvature in the Brillouin zone, the computation is practically demanding because the Berry curvature in many cases a very sharply varying function of k vector. It often strongly depends on contributions from a few ‘*hot spots*’ in the k -space where the spin-orbit-coupling (SOC) causes anti-crossing between bands near the Fermi energy. Such features often require an

extremely dense k -point sampling, and for this reason, the Wannier functions are employed to interpolate the band structure and the wave functions [18]. In Mn₃Sn, the Berry curvature stemming from the Weyl points enhances AHC in the absence of net magnetization [10]. In contrast, in Mn₃PtN, the Berry curvatures spread around the Fermi surfaces in the broad Brillouin-zone region, coming from the band splitting due to the SOC, dominantly contributes to the AHC [17].

Very recently, Naka *et al.* have theoretically examined the possibility of AHE in perovskite transition-metal oxides [19]. It has been predicted that the coexistence of the GdFeO₃-type structural distortion and the collinear AFM configuration gives rise to the AHE by means of the Hubbard model, whereas such unusual AHE has not been experimentally studied so far. One of the candidate materials proposed is CaCrO₃, which is a rare example of a metallic and antiferromagnetic transition-metal oxide. CaCrO₃ crystallizes in orthorhombic *Pbnm* (alternative setting of *Pnma*) perovskite structure. Although CaCrO₃ was previously reported to show semiconducting [20] or insulating [21] properties with the AFM order, recent works have reported its metallic conductivity below the Néel temperature, $T_N = 90\text{K}$ [22, 23]. Powder neutron-diffraction analysis and μSR measurement have revealed that the AFM spin structure is C-type AFM (C-AFM) in which Cr spins order antiferromagnetically in the ab plane but ferromagnetically along the c axis [24, 25]. Owing to the orthorhombic lattice distortion with the metallic collinear AFM ground state, CaCrO₃ is a suitable playground to realize the AHE with no need to consider the complex magnetism such as spin chirality and/or magnetic multipole configurations. In this study, we perform DFT calculations to evaluate the AHC in CaCrO₃ and discuss its microscopic mechanism along with the magnetic symmetry analysis.

II. METHODOLOGY

Density-functional theory (DFT) calculations were performed by using VASP [26] and QUANTUM ESPRESSO [27] packages. The generalized gradient approximation with the parametrization of Perdew, Burke, and Ernzerhof (GGA-PBE) [28] was used for the exchange-correlation functional. The calculations were carried out by following steps. First, the atomic structure was optimized with C-AFM configuration until the atomic force become lower than $0.001\text{eV}/\text{\AA}$ using VASP code with the PAW pseudopotential [29] and then the electronic structure and the magnetic stability were investigated. Secondly, another self-consistency calculation was performed by using QUANTUM ESPRESSO code with the fully relativistic ultrasoft pseudopotentials [30]. The kinetic energy cutoff of 80 Ry and 800 Ry were used for the plane-wave basis set and charge density, respectively. A $12\times 12\times 10$ k -point mesh was taken in the Brillouin zone with the tetrahedron method for integration. Thirdly, we constructed maximally-localized Wannier functions by using WANNIER90 code [31] that is interfaced with the QUANTUM ESPRESSO code. The Wannier functions were built by projections of Bloch wavefunctions onto the localized Cr-3d orbital basis; there are 40 d orbital states in the C-AFM unit cell (4 f.u.). These atomic orbital functions must be carefully chosen otherwise the maximally localization process of the Wannier functions does not converge well. We set up the local (x, y, z) axes in the CrO_6 octahedron by considering the Cr-O bond directions to satisfy the condition: z //long bond, x //short bond, and y //middle bond as possible. The angular functions, $3z^2 - r^2$, zx , yz , $x^2 - y^2$, and xy , were defined in the local coordinates for the Wannier projection. After the Wannier functions were maximally localized, we finally calculated the Berry curvature and the AHC with $120\times 120\times 100$ k -point mesh with $5\times 5\times 5$ adaptive mesh refinement for the turbulent regions.

III. RESULTS AND DISCUSSIONS

A. Electronic and magnetic properties

Figure 1 (a) shows the $Pbnm$ crystal structure of CaCrO_3 with the orthorhombic Brillouin zone and the calculated electronic structure. The metallic state is clearly exhibited by the $2/3$ -filled Cr- t_{2g} state crossing the Fermi energy. Since the t_{2g} level is located away from O- p level and the three-fold degeneracy is not completely lifted due to the lack of strong Jahn-Teller distortion, the t_{2g} state has rather localized character and form the flat bands in the vicinity of the Fermi level. It also appears as a sharp peak, the so-called van Hove singularity, in the DOS, being responsible for the high electric conductivity. In contrast, the e_g orbital state shows a delocalized character as strongly hybridizing with O- p state. The e_g - p bonding state lies in a wide energy range below t_{2g} state

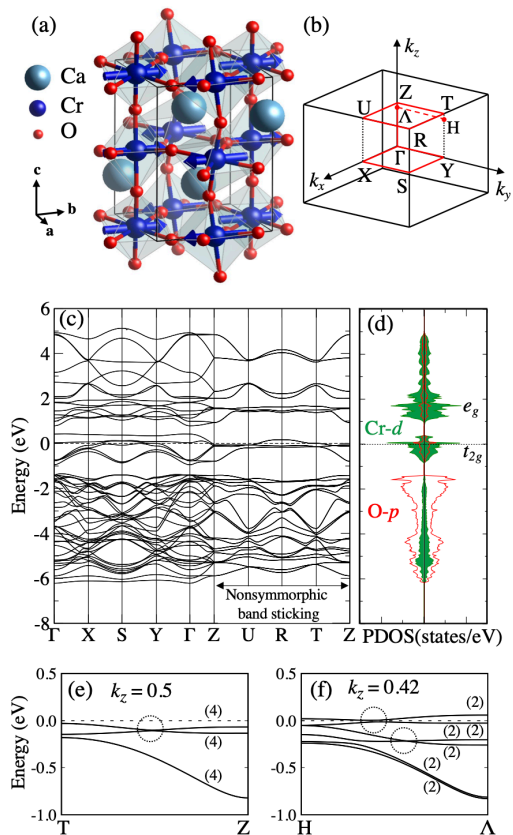


FIG. 1. (a) Orthonormal $Pbnm$ crystal structure of CaCrO_3 with C-AFM spin configuration with Cr spins set parallel to the y axis. (b) First Brillouin zone with the high-symmetry points. (c) Calculated band structure with C-AFM configuration without SOC. (d) Corresponding DOS projected on Cr- d (filled green) and O- p (red) orbital states. (e)(f) The band structure near the Fermi energy along the T-Z line and the H-A lines at $k_z=0.42$, respectively. The number in parentheses is the degeneracy for the band. Fermi energy is set at zero.

and the anti-bonding state spreads above t_{2g} state. The trend is consistent with the previous DFT works.[32, 33]

The nonmagnetic $Pbnm$ space group has eight symmetry operations: $\{E, I, C_{2x} + (\frac{1}{2}\frac{1}{2}0), C_{2y} + (\frac{1}{2}\frac{1}{2}\frac{1}{2}), C_{2z} + (00\frac{1}{2}), m_x + (\frac{1}{2}\frac{1}{2}0), m_y + (\frac{1}{2}\frac{1}{2}\frac{1}{2}), m_z + (00\frac{1}{2})\}$, where E, I, C , and m denote identity, inversion, rotation, and mirror operations, respectively. Three screw and two glide symmetries involving fractional translations manifest the nonsymmorphic space group.

The nonsymmorphic group operations lead to band degeneracies, so-called “band sticking”, across an entire face of the Brillouin zone [34, 35]. Figure 1 (c) illustrates the band sticking effect in the $k_z = 0.5$ plane. Under the C-AFM configuration, all the bands are spin-degenerate at the high-symmetric k points and the additional band-sticking degeneracy is imposed at the Brillouin-zone surfaces. Therefore, two-fold 12 t_{2g} bands become four-fold 6 bands in the Z-U-R-T plane (also see Fig. 2 (a)). The sticking effect causes a narrow bunch of bands just be-

low the Fermi energy along the T-Z line at the $k_z=0.5$ plane (Fig. 1 (e)). Along the H-A line at the $k_z=0.42$ plane, they are split into two groups and the upper-lying bands manifest the band crossing exactly at the Fermi energy (Fig. 1 (f)), forming the nodal lines that will be important later in a following section. Figure 2 shows the band structure projected onto Cr- d orbital states and the Fermi surfaces obtained by using the Wannier-function interpolation. The t_{2g} orbital state are split into xy and $(zx \pm yz)$ orbital states; the latter is a linear combination of two orbital states at neighboring Cr sites. Among them, 5-6th and 7-8th bands form the hole Fermi-surface pockets around the RS line and 9-10th and 11-12th bands form the lotus-flower shaped flat electron Fermi surfaces near the $k_z = 0.5$ plane.

The magnetic stability was examined by comparing the total energy between several magnetic configurations. It is found that C-AFM order shows the total energy lower than those of other spin configurations: ferromagnetic (FM), A-type AFM, and G-type AFM by 209.2, 59.4 and 103.9 meV/f.u., respectively. Taking into account SOC, it is also found that C-AFM order shows the magnetic easy axis along the global y direction. The energy difference is 0.76 meV/f.u. and 0.98 meV/f.u. with respect to the energy with the x and the z spin directions, respectively. Since the magnetic anisotropy energy is very small, hereinafter we will examine the AHC in C-AFM configuration with spins ordered along the x, y , and z axes to compare the values. Then we will focus on the C-AFM order with the y spin orientation to investigate the origin of the AHC in more detail.

B. Magnetic symmetry analysis

When the SOC is involved under the magnetic configuration, the crystalline symmetry is lowered and we must introduce the magnetic space group considering the specified spin direction. In Table I, we show the transformation rules in nonmagnetic space group $Pbnm1'$ considering FM (F), A-type AFM (A), C-type AFM (C), and G-type AFM (G) order parameters with (x, y, z) spin orientation; *e.g.*, C_y indicates the C-AFM order in which the spins are parallel along the global y axis. It is shown that three magnetic order parameters belong to the same irreducible representation, *i.e.*, $\{F_x, C_y, G_z\}$ orders belong to $m\Gamma_2$. It implies that the C_y spin configuration is allowed to cause weakferromagnetic spin canting toward the x direction and weak-antiferromagnetic spin canting with G_z spin component without further symmetry reduction as being consistent with earlier symmetry analyses in Ref. 36–38. This is also consistent with an experimental observation of the C_y ground state with the F_x -type weakferromagnetism in Ref. 24. In addition, it must be noted that the magnetic symmetry allows the finite AHC in C_y or G_z order as well as in F_x order even if the net magnetization is negligible. This is because the physical properties of those three magnetic orders can be

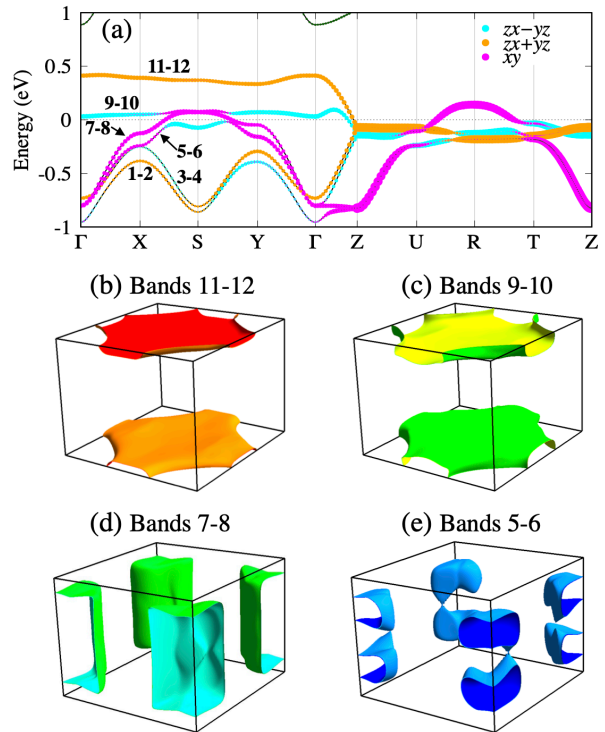


FIG. 2. (a) Wannier-interpolated band structure under the C-AFM configuration projected onto Cr- d orbital states without taking into account of SOC. The band number reflects the AFM spin-degeneracy. The colors highlight the following d -orbital components; magenta denotes d_{xy} , orange denotes d_{zx+yz} , and cyan denotes d_{zx-yz} states. The radii of circles are proportional to the weights of corresponding orbital states. Fermi energy is set at zero. (b-e) Calculated Fermi surfaces with the corresponding band numbers in the orthorhombic Brillouin zone.

regarded equivalent from a symmetry point of view. This unusual symmetry property that AFM order and FM order share the same irreducible representation comes from the nonsymmorphic symmetry operations. For instance, $C_{2x} + (\frac{1}{2}\frac{1}{2}0)$ screw operation flips the y and z spin components located at (000) site and transfers it to $(\frac{1}{2}\frac{1}{2}0)$ site. The transfer between different spin sublattices in the C-AFM configuration makes C_y order invariant under the screw operation as it makes F_x order invariant as well. The symmetry analysis here is also consistent with previous theoretical work on orthorhombic LaCrO_3 , in which the finite FM orbital magnetization and the optical nonreciprocity were predicted in the AFM configurations [38].

The magnetic space group under $\{F_x, C_y, G_z\}$ order is type III $Pbn'm'$ ($Pn'm'a$ in the standard setting), containing four unitary operations $\{E, I, C_{2x} + (\frac{1}{2}\frac{1}{2}0), m_x + (\frac{1}{2}\frac{1}{2}0)\}$ and four antiunitary operations $\{C_{2y}\theta + (\frac{1}{2}\frac{1}{2}\frac{1}{2}), C_{2z}\theta + (00\frac{1}{2}), m_y\theta + (\frac{1}{2}\frac{1}{2}\frac{1}{2}), m_z\theta + (00\frac{1}{2})\}$, where θ de-

notes the antiunitary time-reversal operator.

C. Anomalous Hall conductivity

The AHC was calculated as integrating the Berry curvatures with a summation over the occupied states in the Brillouin zone by WANNIER90 code [31, 40]:

$$\sigma_{\alpha\beta} = -\frac{e^2}{\hbar} \int_{\text{BZ}} \frac{d\mathbf{k}}{(2\pi)^3} \sum_n f_n(\mathbf{k}) \Omega_{n,\alpha\beta}(\mathbf{k}), \quad (1)$$

where n is the band index, α and β are the global Cartesian directions (x, y, z); $\alpha \neq \beta$ for the AHC components and $f_n(\mathbf{k})$ is the occupation factors at the \mathbf{k} point. The Berry curvature was calculated by

$$\Omega_{n,\alpha\beta}(\mathbf{k}) = -2\text{Im} \langle \nabla_{k_\alpha} u_{n\mathbf{k}} | \nabla_{k_\beta} u_{n\mathbf{k}} \rangle \quad (2)$$

in Wannier90 code [31, 41]. Here, $u_{n\mathbf{k}}$ are the cell-periodic Bloch functions for n -th band, projected onto Wannier functions $|\mathbf{R}n\rangle$ by

$$u_{n\mathbf{k}} = \sum_{\mathbf{R}} e^{-i\mathbf{k}\cdot(\mathbf{r}-\mathbf{R})} |\mathbf{R}n\rangle. \quad (3)$$

By applying the conventional perturbation theory, the Berry curvature can be cast into the form of a Kubo-like formula,

$$\Omega_{n,\alpha\beta}(\mathbf{k}) = -2\hbar^2 \text{Im} \sum_{m \neq n} \frac{v_{nm,\alpha}(\mathbf{k}) v_{mn,\beta}(\mathbf{k})}{[\epsilon_m(\mathbf{k}) - \epsilon_n(\mathbf{k})]^2}, \quad (4)$$

where $\epsilon_n(\mathbf{k})$ is the eigenenergy for n -th band at a given \mathbf{k} point and $v_{nm,\alpha}(\mathbf{k})$ is the matrix element of the velocity operator between the occupied n state and the unoccupied m state. The AHC and Berry curvature can be regarded as axial vectors like the spin momentum under the magnetic symmetry operations in their vector form: $\boldsymbol{\sigma} = (\sigma_x, \sigma_y, \sigma_z) = (\sigma_{yz}, \sigma_{zx}, \sigma_{xy})$ and $\boldsymbol{\Omega} = (\Omega_x, \Omega_y, \Omega_z) = (\Omega_{yz}, \Omega_{zx}, \Omega_{xy})$, where n - and k -dependency was omitted for simplicity. Since $\boldsymbol{\Omega}$ is odd with respect to time-reversal symmetry flipping the k vector, the summation of $\boldsymbol{\Omega}$ and accordingly the AHC are zero for non-magnetic materials. Similarly, the symmetry operations transforming k to $-k$ and $\boldsymbol{\Omega}$ to $-\boldsymbol{\Omega}$ simultaneously, the AHC vanishes. Table II shows the transformation of k and $\boldsymbol{\Omega}$ under $\{F_x, C_y, G_z\}$ order; here only summation of Ω_x in k space ($=\sigma_x$) can be non-zero whereas Ω_y and Ω_z cancel out in summation. All the components of AHC vanish if SOC is not considered in the calculations. In the absence of SOC, the spin direction does not affect the orbital nor charge state and hence the spin state is transformed under symmetry operations defined in a black-and-white group (see Appendix A), preventing the spin polarization and AHC in any direction.

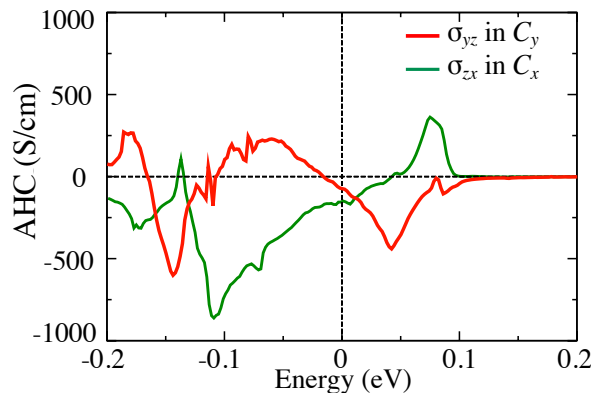


FIG. 3. Calculated AHC tensor components; σ_{yz} in C_y -AFM configuration and σ_{zx} in C_x -AFM configuration as functions of energy. Fermi energy is set to zero.

Figure 3 shows the calculated AHC in C-AFM configuration. All the tensor components were found to be negligible except σ_{yz} in C_y and σ_{zx} in C_x AFM configurations being in agreement with our symmetry analysis (cf. Table I). The values of σ_{yz} and σ_{zx} at Fermi energy were calculated as -74 S/cm and -149 S/cm, respectively.[42] These values are comparable to that in noncollinear AFM Mn_3Sn , reported as $\sigma_{yz}^{\text{DFT}} = 129$ S/cm [43] ($\sigma_{yz}^{\text{EXP}} = 100$ S/cm [6]). Despite the sizable AHC values, CaCrO_3 yields only tiny weakferromagnetic spin canting with the net magnetization $M_x = 0.03 \mu_B/\text{f.u.}$ obtained after optimizing the spin directions in C_y -AFM configuration. This clearly indicates that the conductive electrons sensitively experience the Berry curvature as a fictitious magnetic field in k space instead of the magnetic field caused by the spontaneous magnetization in real space.

The non-monotonous behavior of σ_{yz} and σ_{zx} with respect to the energy is closely associated with the multi-fold t_{2g} band structure around Fermi energy, showing a different trend from the result calculated by a tight-binding model showing simpler energy dependency [19]. In fact, by virtue of the Wannier interpolation, we can quantitatively evaluate the magnitude of AHC that is sensitive to tiny features of the band structure, such as spin-orbit-induced band anti-crossing in a tiny k space volume. The AHC values can be enhanced by shifting the Fermi energy either upward or downward (see Fig. 3). For example, $\sigma_{yz} = -441$ S/cm at $E = E_F + 36$ meV in C_y -AFM and $\sigma_{zx} = 363$ S/cm at $E = E_F + 75$ meV in C_x -AFM configurations. These values are comparable to the AHC value ($\sigma_{xy} \sim 750$ S/cm) calculated in FM bcc Fe, [40, 44] implying the possible enhancement of AHC in CaCrO_3 via chemical doping in practice.

D. Berry curvature and band splitting

In the following, to clarify the microscopic origin of the sizable AHC, we focus on the C_y -AFM configura-

IR of $Pbnm1'$	E	$C_{2x} + (\frac{1}{2}\frac{1}{2}0)$	$C_{2y} + (\frac{1}{2}\frac{1}{2}\frac{1}{2})$	I	θ	Nonzero M component	Nonzero AHC component	Magnetic space group
$m\Gamma_1: A_x, C_z, G_y$	1	1	1	1	-1	-	-	$Pbnm$
$m\Gamma_2: F_x, C_y, G_z$	1	1	-1	1	-1	$-M_x$	σ_{yz}	$Pbn'm'$
$m\Gamma_3: F_y, A_z, C_x$	1	-1	1	1	-1	M_y	σ_{zx}	$Pb'n'm'$
$m\Gamma_4: F_z, A_y, G_x$	1	-1	-1	1	-1	M_z	σ_{xy}	$Pb'n'm'$

TABLE I. Transformation properties in nonmagnetic space group $Pbnm1'$ for FM (F_α) and AFM (A_α, C_α , and G_α) magnetic ordering parameters with $\alpha = x, y, z$ components in the global frame. Only the generators of symmetry operations are shown. The group elements denote the identity, two screws, inversion, and the time reversal. Irreducible representation (IR)'s name is taken from ISODISTORT software [39].

	$\{k_x, k_y, k_z\}$	$\{\Omega_x, \Omega_y, \Omega_z\}$
E	$\{k_x, k_y, k_z\}$	$\{\Omega_x, \Omega_y, \Omega_z\}$
I	$\{-k_x, -k_y, -k_z\}$	$\{\Omega_x, \Omega_y, \Omega_z\}$
C_{2x}	$\{k_x, -k_y, -k_z\}$	$\{\Omega_x, -\Omega_y, -\Omega_z\}$
m_x	$\{-k_x, k_y, k_z\}$	$\{\Omega_x, -\Omega_y, -\Omega_z\}$
$C_{2y}\theta$	$\{-k_x, k_y, -k_z\}$	$\{\Omega_x, -\Omega_y, \Omega_z\}$
$C_{2z}\theta$	$\{-k_x, -k_y, k_z\}$	$\{\Omega_x, \Omega_y, -\Omega_z\}$
$m_y\theta$	$\{k_x, -k_y, k_z\}$	$\{\Omega_x, -\Omega_y, \Omega_z\}$
$m_z\theta$	$\{k_x, k_y, -k_z\}$	$\{\Omega_x, \Omega_y, -\Omega_z\}$

TABLE II. Transformation rules for crystal momentum \mathbf{k} and Berry curvature $\mathbf{\Omega}$ under symmetry operations in $Pbn'm'$ magnetic space group under $\{F_x, C_y, G_z\}$ order. The translation operations in the spiral and glide symmetry operations were removed in the k space.

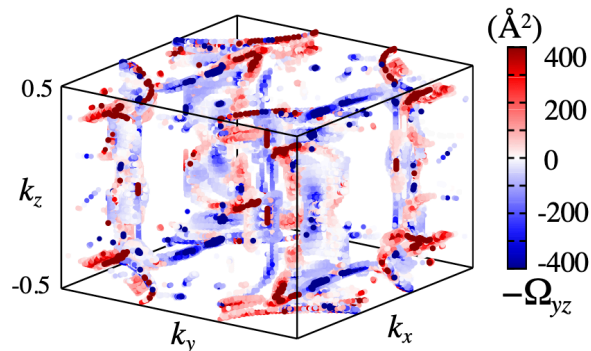


FIG. 4. Distribution of Berry curvatures $-\Omega_{yz}$ (\AA^2) over the octahedral Brillouin zone in C_y -AFM configuration.

tion. Figure 4 shows the distribution of the Berry curvatures Ω_{yz} in the orthorhombic Brillouin zone. It can be seen that the shape formed by high Berry curvature spots resembles some Fermi surfaces (shown in Fig. 2 (b-e)) manifesting that the Berry curvatures stem mainly from the topologically nontrivial points in the vicinity of the Fermi surfaces [45, 46].

Significantly high Berry curvatures were detected at $k_z = 0.42$ plane in the Brillouin zone. As shown in Fig. 5 (a), the high Berry curvatures plot visualizes the hot spots, *i.e.*, two broad lines running parallel to the

k_x axis. These spots are located along the nodal lines opening a small gap near the Fermi energy (cf. Fig. 5 (c) and (e)) and originating from the inter-band interaction between the 11th and 12th bands (also see the corresponding Fermi surfaces at Fig. 2 (b)).

Although one may think that those two bands (*i.e.*, up- and down-spin polarized bands coming from up- and down-spin Cr sites, respectively) were degenerate in the collinear AFM order, the magnetic symmetry in fact allows the spin splitting *even without SOC* at generic k points owing to the effective PT violation; CaCrO_3 can be categorized into SST-4A type like LaMnO_3 in Ref. 47. The spin degeneracy is protected by some symmetry that couples the up-spin and down-spin sites at the higher symmetric k points along the ΛH line ($k_x=0.0$; $-0.5 < k_y < 0.5$; $k_z=0.42$) as shown in Fig. 5 (b) (for the detail symmetry analysis, see Appendix A). On the other hand, at non-symmetric k points ($k_x=0.1$; $-0.5 < k_y < 0.5$; $k_z=0.42$) shown in Fig. 5 (d), the spin degeneracy is lifted even without SOC. A couple of the spin-polarized bands are crossing exactly at the Fermi energy, resulting in the nodal lines. When SOC is turned on, a small gap appears by anticrossing effect and the two bands hybridize across the gap through the SOC interaction. This in turn lets the bands originally having S_y polarization acquire weak S_x polarization as shown in Fig. 5 (e). Simultaneously, Ω_{yz} manifests itself and shows strong enhancement due to the tiny anti-crossing gap along the nodal lines due to Eq. 4. In terms of magnetic symmetry, m_x and $m_y\theta$ symmetry keeps the Ω_{yz} invariant and makes the hot-spot shape symmetric along the k_x and k_y direction in the plane.

E. Effect of structural distortion on anomalous Hall conductivity

As discussed in the preceding section, the non-symmorphic symmetry operation that relates the opposite spin sites in AFM order is a key factor to link the AFM order to FM order and to give rise to the AHE in collinear AFM materials. The orthorhombic crystal structure of CaCrO_3 accommodates a three-dimensional rotation of the octahedra, known as the GdFeO_3 rotation,

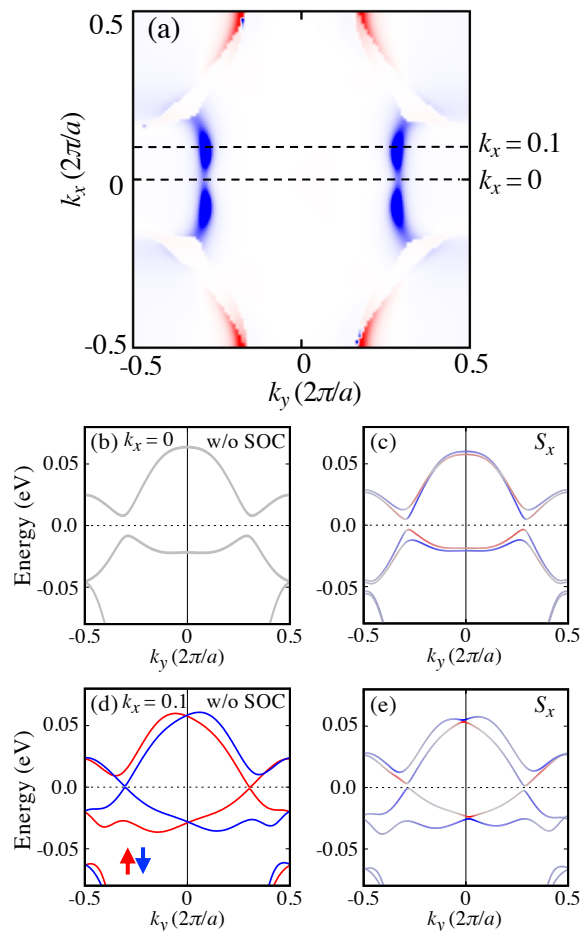


FIG. 5. (a) Color map of Berry curvature Ω_{yz} in $k_z = 0.42$ plane under C_y -AFM configuration. The color range is set same as in Fig. 4. Band structure along the k_y direction corresponding to two dashed lines in (a) in the same plane; (b) and (c) for $k_x = 0$ without SOC and with SOC, respectively; (d) and (e) for $k_x = 0.1$ without SOC and with SOC, respectively. In (c) and (e), the spin polarization along the x direction (S_x) is shown by red and blue colors. In (d), the spin polarization does not have any preferential direction.

concurrently with a Jahn-Teller distortion with respect to the cubic perovskite structure. Considering that the cubic perovskite structure shows symmorphic $Pm\bar{3}m$ space group, we can deduce that the GdFeO_3 rotation drives the AHE and the resulted AHC increases with the distortion.

In order to examine the effect, we performed additional DFT calculations of AHC in MgCrO_3 and SrCrO_3 , replacing A-site cation in CaCrO_3 by smaller and larger elements, respectively. The crystal structures were relaxed starting from CaCrO_3 structure. Table III summarizes the detail of the relaxed structure and the calculated AHC in MgCrO_3 , CaCrO_3 , and SrCrO_3 . The calculated Cr-O-Cr bond angles show that the GdFeO_3 -type octahedral tilting is enhanced in MgCrO_3 and absent in SrCrO_3 . This is consistent with an experimental observation that

SrCrO_3 crystallizes in tetragonal $P4/mmm$ structure [48] while MgCrO_3 structure has not been reported to our best knowledge. The resulted AHC shows that σ_{xy} is zero for SrCrO_3 and σ_{xy} for MgCrO_3 is smaller than that for CaCrO_3 ; the latter is counter-intuitive. In fact, the magnitude of AHC strongly depends on the detail of the band structure near the Fermi energy and therefore it is not directly controlled by tuning the structural distortion. Nevertheless, our result highlights the importance of structural distortion as a driving force of AHE.

	a	b	c	θ	d_{long}	d_{short}	σ_{yz}
MgCrO_3	4.9833	5.1886	7.3030	139.9	1.94	1.91	73.5
CaCrO_3	5.2873	5.3566	7.4985	155.2	1.92	1.91	74.8
SrCrO_3	5.4245	5.4245	7.6639	180.0	1.91	1.91	0.0

TABLE III. Optimized lattice constants a , b , and c (\AA), Cr-O-Cr bond angle in CrO_2 plane θ ($^\circ$), long and short bond distances between Cr and O atoms d_{long} (\AA) and d_{short} (\AA), and calculated AHC σ_{yz} (S/cm) at Fermi energy in $A\text{CrO}_3$ for $A=\text{Mg}$, Ca , and Sr under C_y -AFM order.

IV. SUMMARY

The AHE in CaCrO_3 was predicted by means of first-principles calculation supported by symmetry analysis. The AHC was found to be sizable in the collinear C-AFM as the magnetic ground state and we revealed two essential roles of the non-symmorphic symmetry. (i) The screw and glide symmetry operations bind the AFM and FM order parameters in the same irreducible representation so that AHE is active in the AFM order. (ii) The band-sticking effect at the Brillouin-zone surface makes Cr- t_{2g} state form the narrow bands near the Fermi energy; a couple of those bands cause anticrossing and enhancement of the Berry curvature. We hope that our prediction of AHE in CaCrO_3 will be verified by future experiments. We also expect that our study will provide an important step forward in the understanding of this unusual AHE and in the exploration of related phenomena further in transition-metal oxides with their wide variety of structures and tunable magnetic properties.

ACKNOWLEDGMENTS

We are grateful to M. Naka, M.-T. Suzuki and S. Piccozzi for the fruitful discussions. This work was supported by JST-CREST (Grant No. JPMJCR18T1). The computation in this work has been done using the facilities of the Supercomputer Center, the Institute for Solid State Physics, the University of Tokyo and Supercomputing System MASAMUNE-IMR in the Center for Computational Materials Science, Institute for Materials Research, Tohoku University (Project No. 20K0045). The

crystallographic figure was generated using the VESTA program [49].

Appendix A: Symmetry analysis for spin splitting

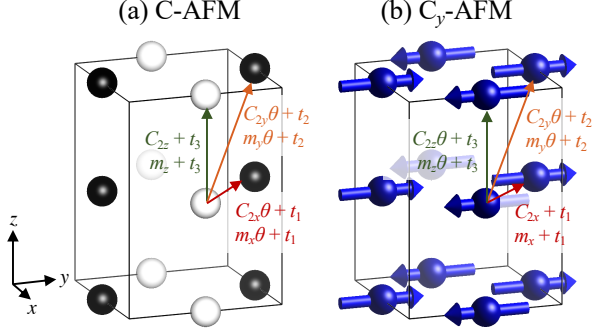


FIG. 6. Screw and glide symmetry operations in (a) C-AFM configuration with black-and-white $Pb'n'm$ space group and (b) C_y -AFM configuration with magnetic $Pbn'm'$ space group. The translation vectors are shown by arrows; $t_1 = (\frac{1}{2}\frac{1}{2}0)$, $t_2 = (\frac{1}{2}\frac{1}{2}\frac{1}{2})$, and $t_3 = (00\frac{1}{2})$.

In crystalline $Pbnm$ space group, there are eight symmetry operations: $\{E, I, C_{2x} + (\frac{1}{2}\frac{1}{2}0), C_{2y} + (\frac{1}{2}\frac{1}{2}\frac{1}{2}), C_{2z} + (00\frac{1}{2}), m_x + (\frac{1}{2}\frac{1}{2}0), m_y + (\frac{1}{2}\frac{1}{2}\frac{1}{2}), m_z + (00\frac{1}{2})\}$. Introducing the time-reversal symmetry θ and adding the products of θ and these eight symmetry operations, it will be nonmagnetic $Pbnm1'$ space group having 16 symmetry operations. By considering an AFM order, the symmetry is reduced according to the spin configuration. When SOC is not taken into account, the spin direction does not have the physical meaning and the spin state shows just two states, *i.e.*, up- and down-spin states. To treat the non-SOC magnetic symmetry, “black-and-white group” is sufficient [50]. As a matter of fact, the black-and-white group is often mixed up with the magnetic space group in the literature. Now we redefine it as follows. Figure 6 (a) shows the C-AFM ordering where different spin sites are shown by black and white spheres. In the black-and-white group, rotation and mirror symmetry operations do not flip the spin, but only the time-reversal symmetry operation θ flips the spins as we turn over a black-and-white disk in the Reversi board game. Therefore, the black-and-white space group has eight symmetry operations: $\{E, I, C_{2z} + (00\frac{1}{2}), m_z + (00\frac{1}{2}), C_{2x}\theta + (\frac{1}{2}\frac{1}{2}0), C_{2y}\theta + (\frac{1}{2}\frac{1}{2}\frac{1}{2}), m_x\theta + (\frac{1}{2}\frac{1}{2}0), m_y\theta + (\frac{1}{2}\frac{1}{2}\frac{1}{2})\}$; we name it black-and-white $Pb'n'm$ space group and distinguish it from the magnetic $Pb'n'm$ space group that appeared in Table I despite the same name. Among those symmetry operations, the latter half accompanies spin-reversal symmetry θ and links the up-spin (black) sites and down-spin (white) sites, hence making two spin states equivalent in the electronic state. In the k space, each k point has the little group of the black-and-white $Pb'n'm$ group,

while the translation part in screw and glide operations is dropped. If the considered k point has one of four symmetries: $\{C_{2x}\theta, C_{2y}\theta, m_x\theta, m_y\theta\}$ originating from the aforementioned screw and glide symmetries, it results in the spin degeneracy of the bands. Hereinafter, we call them “spin-degenerate symmetry operations” for the AFM order. Other symmetry operations in the space group, $\{E, I, C_{2z} + (00\frac{1}{2}), m_z + (00\frac{1}{2})\}$, link the same spin sites and do not cause the spin degeneracy. Obviously, in the FM order, there are no spin-degenerate symmetry operations and hence there is no spin-degeneracy in the band structure.

Γ, X, S									
C-AFM	E	I	C_{2z}	m_z	$C_{2x}\theta$	$C_{2y}\theta$	$m_x\theta$	$m_y\theta$	ss
s	1	1	1	1	-1	-1	-1	-1	no

Γ, X, S									
C_y -AFM	E	I	C_{2x}	m_x	$C_{2y}\theta$	$C_{2z}\theta$	$m_y\theta$	$m_z\theta$	ss
s_x	1	1	1	1	1	1	1	1	yes
s_y	1	1	-1	-1	-1	1	-1	1	no
s_z	1	1	-1	-1	1	-1	1	-1	no

ΓX					ΓS				
C-AFM	E	m_z	$C_{2x}\theta$	$m_y\theta$	ss	C-AFM	E	m_z	ss
s	1	1	-1	-1	no	s	1	1	yes

ΓX					ΓS				
C_y -AFM	E	C_{2x}	$m_y\theta$	$m_z\theta$	ss	C_y -AFM	E	$m_z\theta$	ss
s_x	1	1	1	1	yes	s_x	1	1	yes
s_y	1	-1	-1	1	no	s_y	1	1	yes
s_z	1	-1	1	-1	no	s_z	1	-1	no

TABLE IV. Transformation property of the spin state s and the spin components (s_x, s_y, s_z) at the high symmetric $\Gamma, X,$ and S points and along the high symmetric ΓX and ΓS lines in the orthorhombic Brillouin zone. Without SOC, C-AFM order follows black-and-white $Pb'n'm$ space group and with SOC, C_y -AFM order follows magnetic $Pbn'm'$ space group. The possibility of spin splitting (ss) is shown at the last column.

Here, we demonstrate the symmetry analysis by taking band structure along the ΓX and the ΓS axes as examples; the X and S points are located at $k=(\frac{1}{2}, 0, 0)$ and $(\frac{1}{2}, \frac{1}{2}, 0)$ points in the Brillouin zone, respectively. Table IV shows the transformation properties of spin momenta along these lines. Without SOC, it can be deduced that the ΓX line does not show the spin splitting while the ΓS line shows the spin splitting; the ΓS line holds m_z symmetry in the little group, but it is not the spin-degenerate symmetry operation. In other words, the spin state s is invariant under all the symmetry operations along the ΓS line. This was confirmed in our band structure calculation shown in Fig. 7 (a) and (c). It is interesting to see that the bands are spin-degenerate between the Γ and the X points and largely spin-split between the Γ and the S points without help of SOC. This splitting originates from the AFM configuration that breaks the effective PT symmetry (*i.e.*, product of the space-inversion

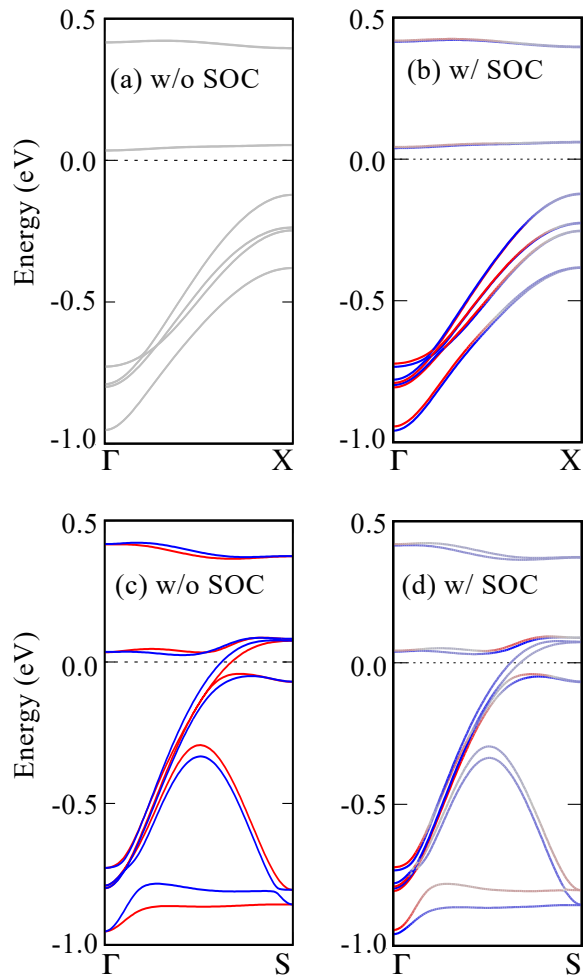


FIG. 7. Calculated band structure (a, b) along the ΓX line and (c, d) along the ΓS line in the orthogonal Brillouin zone. In (a) and (c), SOC is turned off and spin states are shown by red and blue colors. In (b) and (d), SOC is turned on and s_x polarization is shown by red and blue colors. Fermi energy is set as zero energy.

and time-reversal symmetries) [47]. Remind that the spin considered here does not have any preferential direction but just black-and-white states.

When SOC is turned on, the spin direction matters. Considering the spins as axial vectors, the mirror and rotation symmetry operations can flip the spin components (*e.g.*, m_x mirror operation flips s_y and s_z but not s_x) as well as the time-reversal symmetry. By considering C_y -AFM ordering, the nonmagnetic $Pbnm1'$ symmetry is reduced to be $Pbn'm'$ magnetic space group with eight symmetry operations: $\{E, I, C_{2x} + (\frac{1}{2}\frac{1}{2}0), m_x + (\frac{1}{2}\frac{1}{2}0), C_{2y}\theta + (\frac{1}{2}\frac{1}{2}\frac{1}{2}), C_{2z}\theta + (00\frac{1}{2}), m_y\theta + (\frac{1}{2}\frac{1}{2}\frac{1}{2}), m_z\theta + (00\frac{1}{2})\}$. In C_y -AFM order, the spin momenta are collinearly aligned along the y direction and slightly canted towards the x direction. As shown in Table IV, the spin components s_x, s_y, s_z show different symmetry properties. Since C_y -AFM order has the same irreducible

representation as F_x order, s_x is invariant under all the symmetry operations; s_x polarization is allowed to arise everywhere in the k space as spin polarization in FM order. Unlike the AFM-induced spin splitting case, the magnitude of the spin-splitting depends on the magnitude of SOC in this case. As shown in Fig. 7 (b) and (d), the band structure exhibits the additional small band splitting by SOC on top of the non-SOC band structures (*cf.* Fig. 7 (a) and (c)). Along the ΓX axis, s_x polarization is induced by SOC while s_y and s_z polarization is still zero. Along the ΓS axis, s_x is induced by SOC and s_y is induced by AFM order, while s_z is zero. Owing to the weak SOC interaction at Cr $3d$ orbital state, the SOC-induced band splitting is much smaller than the AFM-induced splitting.

The same analysis can apply to the spin-splitting property discussed in Section D. Along the ΛH line, there are $\{E, m_x\theta\}$ symmetry operations originating from the black-and-white space group and the latter protects the spin degeneracy of the band structure without SOC; the degeneracy is lifted by turning on SOC because s_x polarization is allowed by $\{E, m_x\theta\}$ symmetry originating from the magnetic space group as shown in Fig. 5 (b) and (c). Along the non-symmetric k -line, all the spin polarization is allowed with/without SOC as shown in Fig. 5 (d) and (e). For further analysis, information on the other high-symmetric k points and their symmetry in the magnetic space group can be found in the Bilbao Crystallographic Server [51–53]. We confirmed that the spin degeneracy is symmetry-protected along all the k paths in the band structure plot in Fig. 1 (c) without SOC.

Appendix B: Effect of Hubbard U correction

ΔE (meV/f.u)	FM	A-AFM	C-AFM	G-AFM
Bare GGA	209.2	59.4	0	103.9
GGA+ U ($U=3$ eV)	0	12.6	57.5	17.2
GGA+ U ($U=6$ eV)	0	61.8	52.3	52.9

TABLE V. Relative total energy (meV/f.u) calculated with GGA and GGA+ U functionals with $U = 3$ eV and $U = 6$ eV for several spin configurations: FM, A-, C-, and G- type AFM configurations. The lowest energy is highlighted. The crystal structure (both the lattice parameters and the atomic coordinates) was relaxed under C-AFM order and then the total energy was compared by using the VASP code with $12 \times 12 \times 10$ k -point mesh.

In strongly correlated materials, the Hubbard U correction of DFT+ U approach is widely used to reinforce the on-site Coulomb repulsion for $3d$ or $4f$ localized orbital states [54]. Figure 8 shows the change in the electronic state in CaCrO_3 with GGA and GGA+ U potentials with various U values. At bare GGA level (with $U = 0$ eV), the Fermi level crosses the Cr- t_{2g} orbital state showing the good metallic state. As increasing the U value, we found the band-gap opening with $U \gtrsim 2.5$ eV.

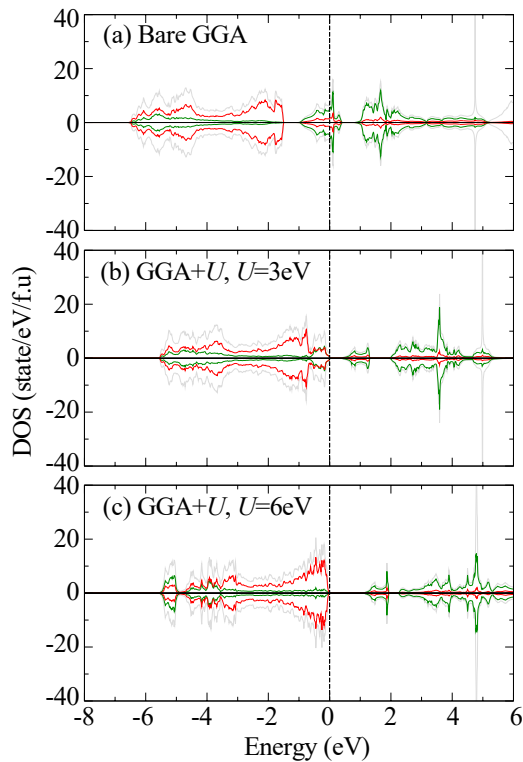


FIG. 8. Calculated total DOS (gray lines) with GGA and GGA+ U functionals with $U = 3$ and 6 eV in C-AFM CaCrO_3 without SOC. Projected DOSs onto Cr- d and O- p orbital states are also shown by green and red lines, respectively.

The band gap increases from 0.3 eV at $U = 3$ eV to 1.0 eV at $U = 6$ eV. This is consistent with the result reported by Streltsov *et al.*; the electronic state is metallic at LSDA level and insulating at LSDA+ U level [32]. Nevertheless, the GGA+ U result is inconsistent with the experimental observations of metallicity in CaCrO_3 [21]. Table V shows the relative total energy for four magnetic configurations with several U values. The bare GGA result correctly reproduces the C-AFM ground state, consistent with the experiment, while GGA+ U results show the wrong solution as the FM ground state. In fact, the Hubbard U correction often overestimates the tendency toward ferromagnetism as already noted by Terakura *et al.* and by Picozzi *et al.* for orthorhombic rare-earth manganites [55, 56]. Considering the better description of the metallic state and the magnetic stability, the bare GGA functional was used in our DFT calculation.

-
- [1] R. Karplus and J. M. Luttinger, *Phys. Rev.* **95**, 1154 (1954).
- [2] H. Chen, Q. Niu, and A. H. MacDonald, *Phys. Rev. Lett.* **112**, 017205 (2014).
- [3] J. Kübler and C. Felser, *EPL (Europhysics Letters)* **108**, 67001 (2014).
- [4] H. Yang, Y. Sun, Y. Zhang, W.-J. Shi, S. S. P. Parkin, and B. Yan, *New Journal of Physics* **19**, 015008 (2017).
- [5] Y. Zhang, Y. Sun, H. Yang, J. Železný, S. P. P. Parkin, C. Felser, and B. Yan, *Phys. Rev. B* **95**, 075128 (2017).
- [6] S. Nakatsuji, N. Kiyohara, and T. Higo, *Nature* **527**, 212 (2015).
- [7] N. Kiyohara, T. Tomita, and S. Nakatsuji, *Phys. Rev. Applied* **5**, 064009 (2016).
- [8] A. K. Nayak, J. E. Fischer, Y. Sun, B. Yan, J. Karel, A. C. Komarek, C. Shekhar, N. Kumar, W. Schnelle, J. Kübler, C. Felser, and S. S. P. Parkin, *Science Advances* **2**, e1501870 (2016).
- [9] J.-Y. Yoon, Y. Takeuchi, S. DuttaGupta, Y. Yamane, S. Kanai, J. Ieda, H. Ohno, and S. Fukami, *AIP Advances* **11**, 065318 (2021).
- [10] T. Chen, T. Tomita, S. Minami, M. Fu, T. Koretsune, M. Kitatani, I. Muhammad, D. Nishio-Hamane, R. Ishii, F. Ishii, R. Arita, and S. Nakatsuji, *Nature Communications* **12**, 572 (2021).
- [11] R. Shindou and N. Nagaosa, *Phys. Rev. Lett.* **87**, 116801 (2001).
- [12] W. Shi, L. Muechler, K. Manna, Y. Zhang, K. Koepfner, R. Car, J. van den Brink, C. Felser, and Y. Sun, *Phys. Rev. B* **97**, 060406(R) (2018).
- [13] L. Šmejkal, R. González-Hernández, T. Jungwirth, and J. Sinova, *Science Advances* **6**, eaaz8809 (2020).
- [14] K. Samanta, M. Ležaić, M. Merte, F. Freimuth, S. Blügel, and Y. Mokrousov, *Journal of Applied Physics* **127**, 213904 (2020), <https://doi.org/10.1063/5.0005017>.
- [15] X. Li, A. H. MacDonald, and H. Chen, *Quantum anomalous hall effect through canted antiferromagnetism* (2019).
- [16] M.-T. Suzuki, T. Koretsune, M. Ochi, and R. Arita, *Phys. Rev. B* **95**, 094406 (2017).
- [17] V. T. N. Huyen, M.-T. Suzuki, K. Yamauchi, and T. Oguchi, *Phys. Rev. B* **100**, 094426 (2019).
- [18] D. Vanderbilt, *Berry Phases in Electronic Structure Theory* (Cambridge University Press, 2018).
- [19] M. Naka, Y. Motome, and H. Seo, *Phys. Rev. B* **106**, 195149 (2022).
- [20] J. Goodenough, J. Longo, and J. Kafalas, *Materials Research Bulletin* **3**, 471 (1968).
- [21] J.-S. Zhou, C.-Q. Jin, Y.-W. Long, L.-X. Yang, and J. B. Goodenough, *Phys. Rev. Lett.* **96**, 046408 (2006).
- [22] E. Castillo-Martínez, A. Durán, and M. Alario-Franco, *Journal of Solid State Chemistry* **181**, 895 (2008).

- [23] J. Weiher, B. Chamberland, and J. Gillson, *Journal of Solid State Chemistry* **3**, 529 (1971).
- [24] A. C. Komarek, S. V. Streltsov, M. Isobe, T. Möller, M. Hoelzel, A. Senyshyn, D. Trots, M. T. Fernández-Díaz, T. Hansen, H. Gotou, T. Yagi, Y. Ueda, V. I. Anisimov, M. Grüninger, D. I. Khomskii, and M. Braden, *Phys. Rev. Lett.* **101**, 167204 (2008).
- [25] O. Ofer, J. Sugiyama, M. Månsson, K. H. Chow, E. J. Ansaldo, J. H. Brewer, M. Isobe, and Y. Ueda, *Phys. Rev. B* **81**, 184405 (2010).
- [26] G. Kresse and J. Furthmüller, *Phys. Rev. B* **54**, 11169 (1996).
- [27] P. Giannozzi, S. Baroni, N. Bonini, M. Calandra, R. Car, C. Cavazzoni, D. Ceresoli, G. L. Chiarotti, M. Cococcioni, I. Dabo, A. D. Corso, S. de Gironcoli, S. Fabris, G. Fratesi, R. Gebauer, U. Gerstmann, C. Gougoussi, A. Kokalj, M. Lazzeri, L. Martin-Samos, N. Marzari, F. Mauri, R. Mazzarello, S. Paolini, A. Pasquarello, L. Paulatto, C. Sbraccia, S. Scandolo, G. Sclauzero, A. P. Seitsonen, A. Smogunov, P. Umari, and R. M. Wentzcovitch, *Journal of Physics: Condensed Matter* **21**, 395502 (2009).
- [28] J. P. Perdew, K. Burke, and M. Ernzerhof, *Phys. Rev. Lett.* **77**, 3865 (1996).
- [29] P. E. Blöchl, *Phys. Rev. B* **50**, 17953 (1994).
- [30] A. Dal Corso, *Computational Materials Science* **95**, 337 (2014).
- [31] A. A. Mostofi, J. R. Yates, Y.-S. Lee, I. Souza, D. Vanderbilt, and N. Marzari, *Computer Physics Communications* **178**, 685 (2008).
- [32] S. V. Streltsov, M. A. Korotin, V. I. Anisimov, and D. I. Khomskii, *Phys. Rev. B* **78**, 054425 (2008).
- [33] H. M. Liu, C. Zhu, C. Y. Ma, S. Dong, and J.-M. Liu, *Journal of Applied Physics* **110**, 073701 (2011).
- [34] Y. Quan, V. Taufour, and W. E. Pickett, *Phys. Rev. B* **105**, 064517 (2022).
- [35] A. Leonhardt, M. M. Hirschmann, N. Heinsdorf, X. Wu, D. H. Fabini, and A. P. Schnyder, *Phys. Rev. Materials* **5**, 124202 (2021).
- [36] D. Treves, *Phys. Rev.* **125**, 1843 (1962).
- [37] E. F. Bertaut, *Acta Crystallographica Section A* **24**, 217 (1968).
- [38] I. V. Solovyev, *Phys. Rev. B* **55**, 8060 (1997).
- [39] B. J. Campbell, H. T. Stokes, D. E. Tanner, and D. M. Hatch, *Journal of Applied Crystallography* **39**, 607 (2006).
- [40] X. Wang, J. R. Yates, I. Souza, and D. Vanderbilt, *Phys. Rev. B* **74**, 195118 (2006).
- [41] M. G. Lopez, D. Vanderbilt, T. Thonhauser, and I. Souza, *Phys. Rev. B* **85**, 014435 (2012).
- [42] We obtained larger AHC value in FM order; $\sigma_{yz} = -150$ S/cm with F_x order in CaCrO_3 .
- [43] M.-T. Suzuki, T. Koretsune, M. Ochi, and R. Arita, *Phys. Rev. B* **95**, 094406 (2017).
- [44] Y. Yao, L. Kleinman, A. H. MacDonald, J. Sinova, T. Jungwirth, D.-S. Wang, E. Wang, and Q. Niu, *Phys. Rev. Lett.* **92**, 037204 (2004).
- [45] X. Wang, D. Vanderbilt, J. R. Yates, and I. Souza, *Phys. Rev. B* **76**, 195109 (2007).
- [46] F. D. M. Haldane, *Phys. Rev. Lett.* **93**, 206602 (2004).
- [47] L.-D. Yuan, Z. Wang, J.-W. Luo, and A. Zunger, *Phys. Rev. Materials* **5**, 014409 (2021).
- [48] A. C. Komarek, T. Möller, M. Isobe, Y. Drees, H. Ulbrich, M. Azuma, M. T. Fernández-Díaz, A. Senyshyn, M. Hoelzel, G. André, Y. Ueda, M. Grüninger, and M. Braden, *Phys. Rev. B* **84**, 125114 (2011).
- [49] K. Momma and F. Izumi, *Journal of Applied Crystallography* **44**, 1272 (2011).
- [50] G. Burns, *Introduction to Group Theory with Applications* (Academic Press, 1977).
- [51] M. Aroyo, J. Perez-Mato, D. Orobengoa, E. Tasci, G. De La Flor, and A. Kirov, *Bulgarian Chemical Communications* **43**, 183 – 197 (2011), cited by: 421.
- [52] M. I. Aroyo, J. M. Perez-Mato, C. Capillas, E. Kroumova, S. Ivantchev, G. Madariaga, A. Kirov, and H. Wondratschek, *Zeitschrift für Kristallographie - Crystalline Materials* **221**, 15 (2006).
- [53] M. I. Aroyo, A. Kirov, C. Capillas, J. M. Perez-Mato, and H. Wondratschek, *Acta Crystallographica Section A* **62**, 115 (2006).
- [54] S. L. Dudarev, G. A. Botton, S. Y. Savrasov, C. J. Humphreys, and A. P. Sutton, *Phys. Rev. B* **57**, 1505 (1998).
- [55] I. Solovyev, N. Hamada, and K. Terakura, *Phys. Rev. B* **53**, 7158 (1996).
- [56] S. Picozzi, K. Yamauchi, G. Bihlmayer, and S. Blügel, *Phys. Rev. B* **74**, 094402 (2006).